VI International Conference on Particle-based Methods – Fundamentals and Applications
PARTICLES 2019
E. Oñate, M. Bischoff, D.R.J. Owen, P. Wriggers & T. Zohdi (Eds)

A LATTICE BOLTZMANN METHOD IN GENERALIZED CURVILINEAR COORDINATES

J. A. Reyes Barraza[1] and R. Deiterding[2]

[1] Aerodynamics and Fluid Mechanics Research Group
Engineering and Physical Sciences Faculty
University of Southampton
Highfield Campus, Southampton SO17 1BJ, UK
Email: j.a.reyes@soton.ac.uk

[2] Aerodynamics and Fluid Mechanics Research Group
Engineering and Physical Sciences Faculty
University of Southampton
Highfield Campus, Southampton SO17 1BJ, UK
Email R.Deiterding@soton.ac.uk, Web page: http://rdeiterding.website/

Key words: LBM, Generalized Curvilinear Coordinates, Finite Difference

Abstract. A second-order central time-explicit method is implemented to solve the Lattice Boltzmann Equation in generalized curvilinear coordinates in order to simulate fluid flows with non-uniform grids and curved boundaries. Several test cases are used for verification, including the Taylor-Green vortex in two-dimensions, the square lid-driven cavity and the 2D circular cylinder. The Taylor-Green vortex is a classical benchmark test that is compared with the analytical solution using a non-uniform grid. The 2D lid-driven cavity is solved for moderate Reynolds numbers, where a clustering function is employed to stretch the mesh and increase the resolution in the cavity corners. The boundary conditions for these two test-cases are relatively straightforward to implement since there are no curved walls. Therefore, the 2D circular cylinder is used to demonstrate the capacity of the present method to perform steady and unsteady simulations with curved boundaries. Our results have been compared with the literature available, and the outcomes of this method are consistent with other results, confirming the feasibility of the implemented scheme. In addition, the present method has been compared to our own standard Cartesian lattice Boltzmann solver with adaptive mesh refinement for the 2D circular cylinder problem.

1 INTRODUCTION

The lattice Boltzmann method (LBM) is a relatively new development, that has emerged as a powerful computational method for the study of fluid dynamic problems. Instead of approximating the Navier-Stokes equations, the approach is based on solving a simplified version of the Boltzmann equation in a specific discrete space. It can be shown via the Chapman-Enskog expansion that the LBM recovers the Navier-Stokes equations in the nearly incompressible flow limit [1]. The simplicity of the lattice Boltzmann algorithm can lead to dramatic reductions in computational time compared to traditional computational fluid dynamics (CFD) solvers. On uniform grids and unsteady flow simulations, it can easily show performance gains up to two orders of magnitude [2], which has made the approach certainly popular in recent years.

In the standard LBM, the discretisation of the physical space is coupled with the discretisation of momentum space [3]. The advantage of this scheme is the exact treatment of the advection term, therefore it does not have any numerical diffusion. On the other hand, this condition results in a numerical method that is restricted to Cartesian grids. This aspect of the standard LBM limits its application and solving problems with curved geometries and thin boundary layers become troublesome. For realistic geometries and aerodynamic investigations, the usage of uniform Cartesian meshes is impractical, since the boundary layer flow needs to be adequately resolved for a good representation of the physics. It is somewhat straightforward to apply isotropic mesh adaptation to the standard LBM, and thereby resolving laminar boundary layers is relatively easy [4]. However, this approach can become remarkably expensive for capturing boundary layers of turbulent flows, and therefore it is impractical for most technically relevant problems in aerodynamics.

The discretisation of the physical space does not necessarily require to be coupled with the moment space [5]. Therefore, it is possible to implement standard numerical techniques on the LBM to use non-uniform and body-fitted meshes. In recent years, several efforts have been made to overcome this shortcoming in order to make LBM a practical computational fluid dynamics tool. Some authors have taken different approaches toward the same issue. Some of them have used interpolation schemes [6] and others have applied traditional numerical methods used in CFD mainly, finite differences [7] and finite volume [8]. Therefore, we propose an implementation of the LBM in generalized curvilinear coordinates, so the LBE can be solved with non-Cartesian grids. Various test cases were used for verification, including the Taylor green vortex, the 2D lid-driven cavity and the 2D circular cylinder. Clustering functions are employed on all test-cases to stretch the mesh and increase resolution on certain regions of the domains. This study shows that this implementation deals with curved boundary walls more accurately and efficiently than the Cartesian method.

2 METHODOLOGY

In this paper, the implementation is done on the classical D2Q9 LBM-BGK model [1]. Hence, the LBE with a simplified collision operator can be written as

$$\frac{\partial f_\alpha}{\partial t} + \mathbf{e}_\alpha \cdot \nabla f_\alpha = -\frac{1}{\tau}\left(f_\alpha - f_\alpha^{eq}\right). \tag{1}$$

The latter can be transformed into a generalized curvilinear coordinate system, in which the physical and computational planes are represented by (x, y) and $(\xi,\, \eta)$, respectively,

$$\begin{aligned} \xi &= \xi(x, y), \\ \eta &= \eta(x, y). \end{aligned} \tag{2}$$

To transform the LBE from the physical plane (x, y) to the computational plane $(\xi,\, \eta)$ we must apply

$$\begin{aligned} \frac{\partial}{\partial x} &= \frac{\partial}{\partial \xi}\frac{\partial \xi}{\partial x} + \frac{\partial}{\partial \eta}\frac{\partial \eta}{\partial x}, \\ \frac{\partial}{\partial y} &= \frac{\partial}{\partial \xi}\frac{\partial \xi}{\partial y} + \frac{\partial}{\partial \eta}\frac{\partial \eta}{\partial y}. \end{aligned} \tag{3}$$

The physical domain is related to the computational domain by the following condition

$$\begin{bmatrix} \xi_x & \xi_y \\ \eta_x & \eta_y \end{bmatrix} = \frac{1}{J}\begin{bmatrix} y_\eta & -x_\eta \\ -y_\xi & x_\xi \end{bmatrix}, \tag{4}$$

where J is the Jacobian of the transformation defined as

$$J = x_\xi y_\eta - x_\eta y_\xi. \tag{5}$$

The convection term in Eq. (1) can be rewritten as

$$\begin{aligned} \mathbf{e}_\alpha \cdot \nabla f_\alpha &= e_{\alpha x}\frac{\partial f_\alpha}{\partial x} + e_{\alpha y}\frac{\partial f_\alpha}{\partial y} \\ &= e_{\alpha x}\left(\frac{\partial f_\alpha}{\partial \xi}\frac{\partial \xi}{\partial x} + \frac{\partial f_\alpha}{\partial \eta}\frac{\partial \eta}{\partial x}\right) + e_{\alpha y}\left(\frac{\partial f_\alpha}{\partial \xi}\frac{\partial \xi}{\partial y} + \frac{\partial f_\alpha}{\partial \eta}\frac{\partial \eta}{\partial y}\right) \\ &= \left(e_{\alpha x}\frac{\partial \xi}{\partial x} + e_{\alpha y}\frac{\partial \xi}{\partial y}\right)\frac{\partial f_\alpha}{\partial \xi} + \left(e_{\alpha x}\frac{\partial \eta}{\partial x} + e_{\alpha y}\frac{\partial \eta}{\partial y}\right)\frac{\partial f_\alpha}{\partial \eta} \\ &= \tilde{e}_{\alpha\xi}\frac{\partial f_\alpha}{\partial \xi} + \tilde{e}_{\alpha\eta}\frac{\partial f_\alpha}{\partial \eta}, \end{aligned} \tag{6}$$

where

$$\tilde{\mathbf{e}}_\alpha = (\tilde{e}_{\alpha\xi}, \tilde{e}_{\alpha\eta}) = (e_{\alpha x}\xi_x + e_{\alpha y}\xi_y, e_{\alpha x}\eta_x + e_{\alpha y}\eta_y). \tag{7}$$

Therefore, the LBE in the computational domain can be written as

$$\frac{\partial f}{\partial t} + \tilde{e}_{\alpha\xi}\frac{\partial f_\alpha}{\partial \xi} + \tilde{e}_{\alpha\eta}\frac{\partial f_\alpha}{\partial \eta} = -\frac{1}{\tau}\left(f_\alpha - f_\alpha^{eq}\right). \tag{8}$$

Equation (8) can be solved using any appropriate numerical procedure. The spatial derivatives are discretised by the second-order central difference and the temporal term is integrated by the explicit multistage Runge-Kutta. The right hand side of Eq. (8) can be rewritten as

$$R_{\alpha_{(i,j)}} = -\left(\tilde{e}_{\alpha\xi_{(i,j)}}\frac{f_{\alpha_{(i+1,j)}} - f_{\alpha_{(i-1,j)}}}{2\Delta\xi} + \tilde{e}_{\alpha\eta_{(i,j)}}\frac{f_{\alpha_{(i,j+1)}} - f_{\alpha_{(i,j-1)}}}{2\Delta\eta}\right) - \frac{1}{\tau}\left(f_{\alpha_{(i,j)}} - f^{eq}_{\alpha_{(i,j)}}\right). \tag{9}$$

Now, the solution is advanced in the time by using the standard fourth-stage Runge-Kutta scheme as follows,

$$\begin{aligned} f^1_\alpha &= f^t_\alpha, \\ f^2_\alpha &= f^1_\alpha + \frac{\Delta t}{4}R^1_\alpha, \\ f^3_\alpha &= f^1_\alpha + \frac{\Delta t}{3}R^2_\alpha, \\ f^4_\alpha &= f^1_\alpha + \frac{\Delta t}{2}R^3_\alpha, \\ f^{t+\Delta t}_\alpha &= f^1_\alpha + \Delta t R^4_\alpha. \end{aligned} \tag{10}$$

Central schemes can be unstable when non-linearities are present. Therefore a fourth-order artificial dissipation is added in Eq. (9) as

$$D = -\epsilon\left((\Delta\xi)^4\frac{\partial^4 f_\alpha}{\partial\xi^4} + (\Delta\eta)^4\frac{\partial^4 f_\alpha}{\partial\eta^4}\right), \tag{11}$$

in order to stabilize the solution [9]. The order of the numerical scheme does not change since the artificial dissipation has a higher order than the formal scheme.

3 COMPUTATIONAL RESULTS

Numerical computations are carried out to show that the second-order central time-explicit method implemented is an accurate, stable and reliable option to solve the LBE in curvilinear coordinates. Also, to demonstrate its superior capabilities to resolve the flow in the vicinity of the wall when using curved geometries.

3.1 Taylor-Green vortex

The Taylor-Green vortex decay problem has been widely used for the verification of incompressible flow solvers. This problem has an exact solution of the incompressible Navier-Stokes equations and the set-up is straightforward, since it only has a set of initial conditions and periodic boundaries. This benchmark test is done to demonstrate the accuracy of the scheme, and the capacity of the present methodology to use non-uniform

grids. The exact solution of this unsteady problem is given by

$$\begin{aligned} u(x,y,t) &= -u_o \cos(k_x x)\sin(k_y y)e^{-k^2\nu t}, \\ v(x,y,t) &= \frac{k_x}{k_y} u_o \sin(k_x x)\cos(k_y y)e^{-k^2\nu t}, \\ P(x,y,t) &= P_0 - 0.25\rho_0 u_o^2 \left[\cos(2k_x x) + \left(\frac{k_x}{k_y}\right)^2 \cos(2k_y y)\right] e^{-2k^2\nu t}, \end{aligned} \tag{12}$$

where u_o is the initial velocity magnitude, ν is the kinematic viscosity of the fluid, $k_x = 2\pi/L_x$ and $k_y = 2\pi/L_y$ are the wave numbers in x and y directions, $k = \sqrt{k_x^2 + k_y^2}$, The initial conditions for the velocity and pressure fields are obtained by setting $t = 0$.

A clustering function has been selected to stretch the mesh in both directions, x and y. The stretched grid can be obtained with:

$$x = H\frac{(2\alpha+\beta)[(\beta+1)/(\beta-1)]^{(\xi-\alpha)/(1-\alpha)} + 2\alpha - \beta}{(2\alpha+1)\left(1+[(\beta+1)/(\beta-1)]^{(\xi-\alpha)/(1-\alpha)}\right)}, \tag{13}$$

$$y = H\frac{(2\alpha+\beta)[(\beta+1)/(\beta-1)]^{(\eta-\alpha)/(1-\alpha)} + 2\alpha - \beta}{(2\alpha+1)\left(1+[(\beta+1)/(\beta-1)]^{(\eta-\alpha)/(1-\alpha)}\right)}, \tag{14}$$

where β is the clustering parameter, α defines where the clustering takes place, and H is the length. If $\alpha = 0.5$, the clustering is distributed equally, and if $\alpha = 0$ the clustering takes place at H. Herein, all the computations are performed with $\alpha = 0.5$ and $\beta = 1.2$.

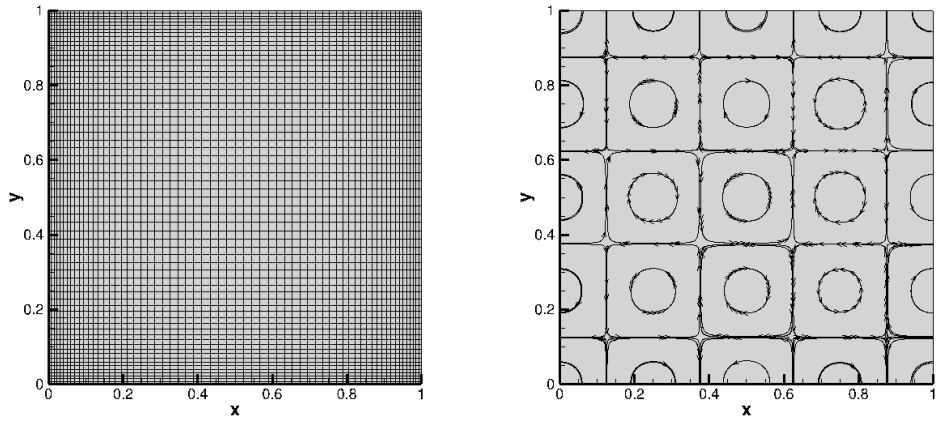

Figure 1: Left: Non-uniform mesh. Right: Streamlines for the Taylor-Green Vortex at the initial conditions.

Figure (1) shows the non-uniform grid, namely (65×65), that can be obtained by applying the clustering functions described, and the initial flow field shown by streamlines. The present methodology is compared with the analytical solution and shown in Figure (2) at a dimensionless time of 0.2. For this simulation a grid of (128×128) was used, the reference velocity u_o is 0.02 and a Reynolds number of 100 was selected.

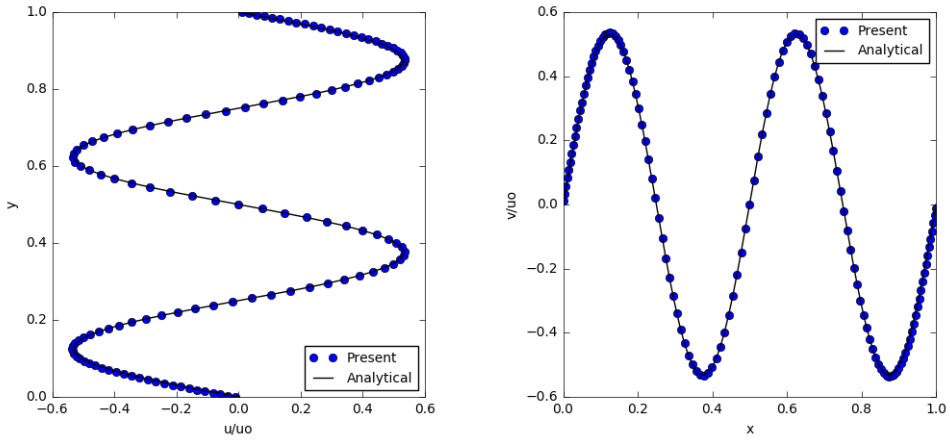

Figure 2: Left: u-velocity along the vertical centreline. Right: v-velocity along the horizontal centreline.

3.2 2D lid-driven cavity

The 2D lid-driven cavity is a classical benchmark test, thanks to its simple geometry and complex flow physics [10]. It consists of the movement of the top-lid at a constant velocity (u_o) and three stationary walls ($u = v = 0$). The geometry normally is a square of aspect ratio one, but this may be different. The same grid (cf. Fig. 1) used for the Taylor-Green vortex is also used for this test case. The numerical computations are carried out with $u_o = 0.1$ and the results are shown for two different Reynolds numbers, Re = 1000 and Re = 3200. The grid sizes used are (257×257) and (513×513) respectively.

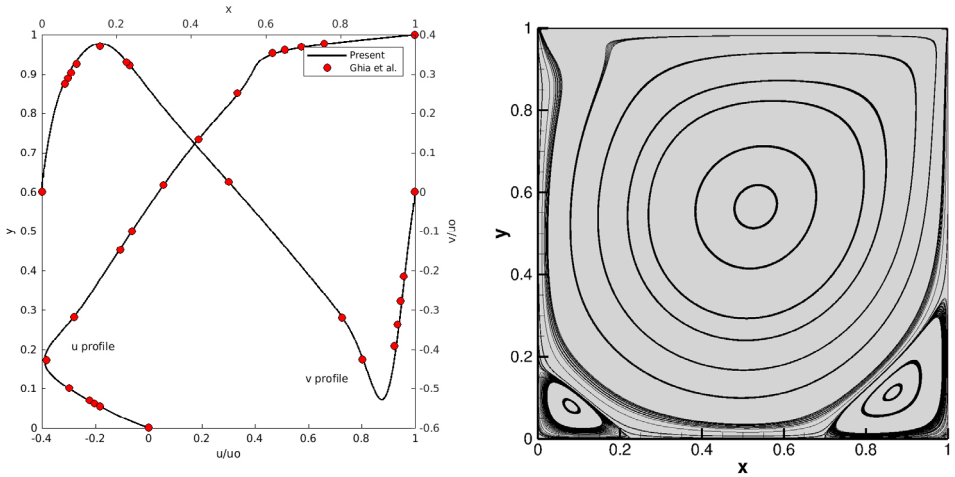

Figure 3: Re = 1000. Left: u-velocity along the vertical centreline and v-velocity along the horizontal centreline. Right: Flow field exhibited by streamlines.

There is no exact solution for the 2D cavity flow, because of this we need to compare our results with a comprehensive study, such as the one done by Ghia et al. [10]. The

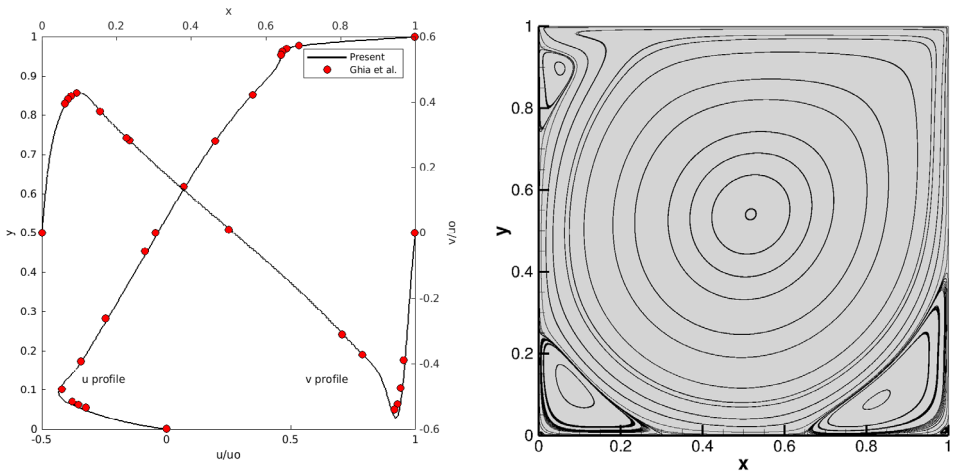

Figure 4: Re = 3200. Left: u-velocity along the vertical centreline, v-velocity along the horizontal centreline. Right: Flow field exhibited by streamlines.

u-velocity profile along the vertical centre line, the v-velocity profile along the horizontal centre line and the streamlines for the two different Reynolds numbers are shown in Figures 3 and 4. This shows that our results have an excellent agreement with the reference [10], and the streamlines show a correct flow behaviour in the entire domain. It is known that the corners are singularity points, and our results do not exhibit any issue in this regions, demonstrating the capability of the current methodology and the proper application of the stretching function on the grid.

3.3 2D circular cylinder

The wall-boundary treatment of the previous test cases is relatively straightforward since there are no curved walls. Therefore, the 2D circular cylinder is used to demonstrate the capacity of the present method to perform steady and unsteady simulations with curved surfaces. In addition, proper stretching functions have been implemented to increase the resolution in the proximity of the wall and in the wake region. Our results have been compared with the literature available, and the outcomes of the present method are consistent with other results, supporting the proposed scheme. In addition, the present method is compared to our own standard Cartesian LBM solver [2], AMROC (Adaptive Mesh Refinement in Object-oriented C++).

The following function is used for the stretching in the wall normal direction

$$y_n = \delta \frac{(1-\beta)\left(\frac{\beta+1}{\beta-1}\right)^{1-\xi} + (\beta+1)}{\left(\frac{\beta+1}{\beta-1}\right)^{1-\xi} + 1} + r, \quad 0 \leq \xi \leq 1, \tag{15}$$

where δ is the radial distance between the body and the outer boundary, β is the clustering parameter which has been set to 1.007 for these simulations and r is the radius of the cylinder. The grid clustering function shown in Eq.(14) was used to increase the resolution

behind the cylinder. The clustering parameter used for the wake is 1.045.

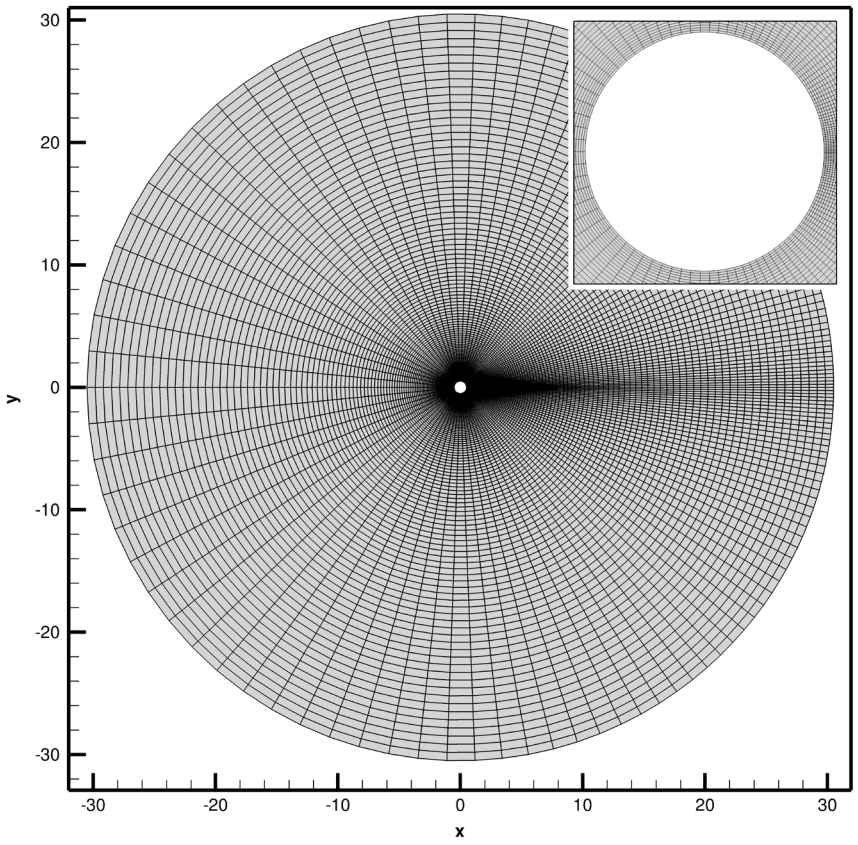

Figure 5: O-Grid for the 2D cylinder mesh. Overlaid on the upper-right is a close-up of the body-conforming mesh around the cylinder.

All the computations for the cylinder test-case using the proposed methodology were carried out on a grid size of (257×257) with an outer diameter 30 times bigger than the inner diameter (cf. Fig. 5). The simulations carried out using the Cartesian LBM with adaptive mesh refinement were performed on a domain size of $[-16D \times 48D] \times [-16D \times 16D]$ with the axis located at $(x, y) = (0, 0)$ and using a grid size of (640×320) at its coarsest level (for the steady-state cases). The adaptive mesh refinement is set to 3 additional levels with a refinement factor of 4.

Two Reynolds number were selected for the steady-state simulations, 20 and 40. At this flow regime a stationary recirculation region appears for both cases behind the cylinder, and the wake increases in length as the Reynolds number increases, as it can be seen in Figure 6. The literature shows that the recirculating regions appear around $5 < \mathrm{Re} < 47$. Anything under Reynolds number 5 the flow will remain attached and above the critical Reynolds, which is 47, the solution produced will be unsteady.

The comparison of the steady-state results are shown in Table 1. The references used are quite vast and they include the numerical solutions of the Navier-Stokes equations from

Table 1: Effects of the Reynolds number on steady flow over the circular cylinder

Re	Author(s)	C_d	$C_p(0)$	$C_p(180)$	$2L/D$
20	Tritton [11]	2.10	-	-	-
	Henderson [12]	2.06	-	-0.60	-
	Dennis and Chang [13]	2.05	1.27	-0.58	1.88
	Hejranfar and Ezzatneshan [5]	2.02	1.25	-0.59	1.84
	AMROC-LBM	1.98	1.26	-0.59	1.85
	Present	2.02	1.31	-0.55	1.85
40	Tritton [11]	1.59	-	-	-
	Henderson [12]	1.55	-	-0.53	-
	Dennis and Chang [13]	1.52	1.14	-0.50	4.69
	Hejranfar and Ezzatneshan [5]	1.51	1.15	-0.48	4.51
	AMROC-LBM	1.45	1.19	-0.49	4.66
	Present	1.51	1.19	-0.46	4.60

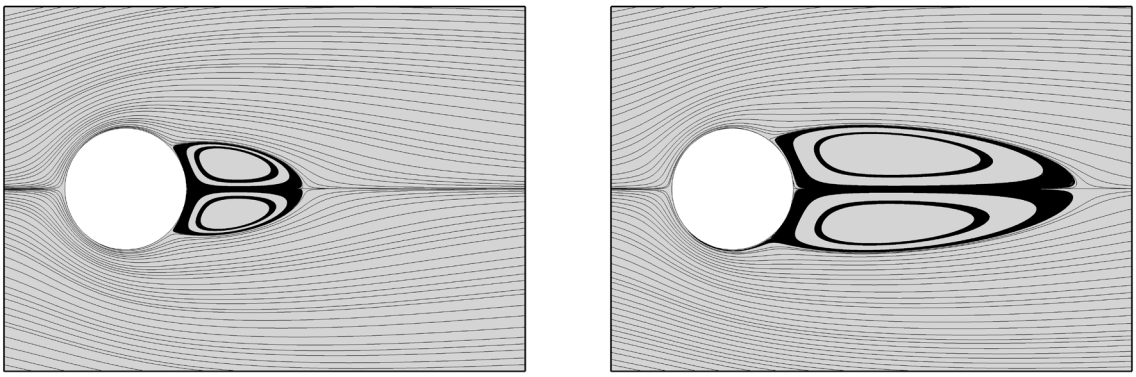

Figure 6: Flowfield for steady flow over the 2D circular cylinder shown by streamlines using the implemented methodology. Left: Re = 20. Right: Re = 40.

Henderson [12], Dennis and Chang [13], compact-finite difference LBM from Hejranfar and Ezzatneshan [5] and the experimental data from Tritton [11]. The variables presented are drag coefficient C_d, the pressure coefficient at the stagnation point $C_p(0)$ and at the rear-point $C_p(180)$, the normalized length of the wake $2L/D$, where L is the actual length of the wake and D is the diameter of the cylinder. Table 1 shows that our results exhibit good agreement with diverse references.

For the unsteady test-case, two laminar flows at 100 and 200 Reynolds number were selected. These simulations demonstrate the capacity of the presented method to simulate time-dependent flows around geometries with curved boundaries. At these flow conditions, the recirculation bubbles behind the cylinders become unstable, and time-periodic vortex-shedding solutions appear. The dimensionless number used to characterize this phenomenon is the Strouhal number that is defined as $St = f_q D/u_o$, where f_q is the

shedding frequency. The Strouhal number can also be written as $St = D/u_o T_p$, where T_p is the peak-to-peak period of the lift coefficient.

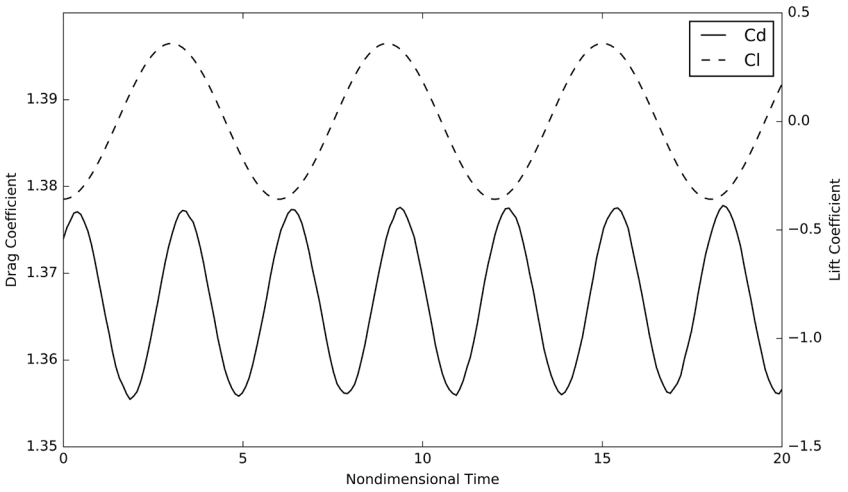

Figure 7: Drag and lift coefficient trends for the time periodic flow over the circular cylinder at Re = 100.

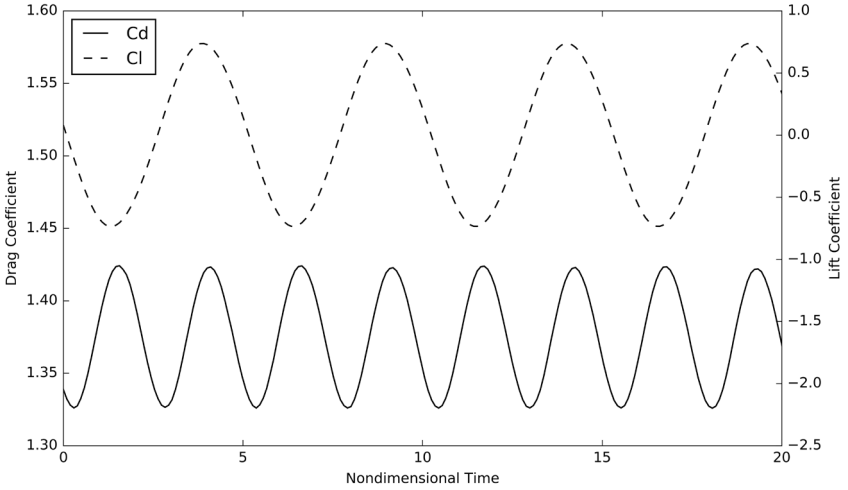

Figure 8: Drag and lift coefficient trends for the time periodic flow over the circular cylinder at Re = 200.

The lift and drag coefficient with respect to the non-dimensional time are shown in Figures 7 and 8, after the simulations have reached a stable periodic solution. These plots show the capacity of the central-scheme implemented to predict correctly the vortex-shedding phenomenon within these Reynolds numbers. Table 2 compares the present time-depended solutions with the reference selected and as well as with the results obtained using AMROC-LBM. The Navier-Stokes solutions from Chiu et al. [14] are used as a

Table 2: Strouhal number for different authors

Re	Author(s)	St	$\overline{C_d}$	C_l'
100	Chiu et al. [14]	0.167	1.35	0.30
	AMROC-LBM	0.165	1.25	0.30
	Present	0.165	1.36	0.35
200	Chiu et al. [14]	0.198	1.37	0.71
	Present	0.196	1.37	0.73

reference. The variables compared are the Strouhal number, the average drag coefficient $\overline{C_d}$ and the lift coefficient amplitude C_l'. The results produced by the LBM in generalized curvilinear coordinates have an excellent agreement with the references for all the variables compared. The results obtained by AMROC-LBM also have a good agreement with the variables compared. However, in this case it was necessary to increase the resolution to (960×480) at its coarsest level, the domain and the mesh adaptation settings remained the same, in order to get convergence.

4 CONCLUSIONS

It is noticeable that the Cartesian solver requires a significantly higher number of grid points in order to obtain a converged solution, given its inability to represent curved geometries accurately and its lack of flexibility to have meshes of diverse sizes. On the other hand, it is possible to apply isotropic mesh adaptation and to benefit from it. In this study, it has been shown that the second-order scheme implemented is accurate, stable and capable of solving the LBE in generalized curvilinear coordinates. The results obtained by the present methodology and AMROC-LBM exhibit good agreement with all references. However, the current implementation deals with curved boundary walls more accurately and efficiently than the Cartesian method.

The test cases in this paper are relevant to the literature and serve well to validate the current implementation. However, it is within our scope to solve more technically challenging problems. Hence as a next step, it is planned to solve the flows around aerofoils, which require a high-level of mesh stretching for properly resolving the boundary layer.

5 ACKNOWLEDGEMENTS

The authors gratefully acknowledge the support of CONACYT (Consejo Nacional de Ciencia y Tecnología), CVU: 526498.

References

[1] S. Chen, G. D. Doolen, Lattice Boltzmann method for fluid flows, Annual Review of Fluid Mechanics 30 (1998) 329–364.

[2] R. Deiterding, S. L. Wood, Predictive wind turbine simulation with an adaptive

lattice Boltzmann method for moving boundaries, Journal of Physics: Conference Series 753 (2016).

[3] X. He, L.-S. Luo, Theory of the lattice Boltzmann method: From the Boltzmann equation to the lattice Boltzmann equation, Physical Review E 56 (1997) 6811–6817.

[4] Z. Guo, C. Shu, Lattice Boltzmann Method and its Applications in Engineering, World Scientific, 2013.

[5] K. Hejranfar, E. Ezzatneshan, Implementation of a high-order compact finite-difference lattice Boltzmann method in generalized curvilinear coordinates, Journal of Computational Physics 267 (2014) 28–49.

[6] X. He, G. Doolen, Lattice Boltzmann method on curvilinear coordinates system: Flow around a circular cylinder, Journal of Computational Physics 134 (1997) 306–315.

[7] R. Mei, W. Shyy, On the finite difference-based lattice Boltzmann method in curvilinear coordinates, Journal of Computational Physics 143 (1998) 426–448.

[8] S. Succi, G. Amati, R. Benzi, Challenges in lattice Boltzmann computing, Journal of Statistical Physics 81 (1995) 5–16.

[9] K. Hejranfar, M. Hajihassanpour, Chebyshev collocation spectral lattice Boltzmann method in generalized curvilinear coordinates, Computers and Fluids 146 (2017) 154–173.

[10] U. Ghia, K. N. Ghia, C. T. Shin, High-resolutions for incompressible flows using Navier-Stokes equations and a multigrid method, Journal of Computational Physcis 48 (1982) 387–411.

[11] D. Tritton, Experiments on the flow past a circular cylinder at low Reynolds numbers, Journal of Fluid Mechanics 6 (1959) 547–567.

[12] R. D. Henderson, Details of the drag curve near the onset of vortex shedding, Physics of Fluids 7 (1995) 2102–2104.

[13] S. C. R. Dennis, G. Chang, Numerical solutions for steady flow past a circular cylinder at Reynolds numbers up to 100, Journal of Fluid Mechanics 42 (1970) 471–489.

[14] P. H. Chiu, R. K. Lin, T. W. Sheu, A differentially interpolated direct forcing immersed boundary method for predicting incompressible Navier Stokes equations in time-varying complex geometries, Journal of Computational Physics 229 (2010) 4476–4500.